Spectrochimica Acta Part A: Molecular and Biomolecular Spectroscopy 322 (2024) 124684

Contents lists available at ScienceDirect

Spectrochimica Acta Part A: Molecular and Biomolecular Spectroscopy

journal homepage: www.journals.elsevier.com/spectrochimica-acta-part-a-molecular-and-biomolecular-spectroscopy

# Molecular mechanisms behind BRACO19 and human telomeric G-quadruplex interaction

Valeria Libera [a,1], Claudia Fasolato [b,1], Francesca Ripanti [a,2], Sara Catalini [a,c,d], Luca Bertini [a], Caterina Petrillo [a], Giorgio Schirò [e], Francesco D'Amico [f], Barbara Rossi [f], Alessandro Paciaroni [a], Lucia Comez [g,*]

[a] Department of Physics and Geology, University of Perugia, via Alessandro Pascoli, 06123, Perugia, Italy
[b] Institute for Complex System, National Research Council (ISC-CNR), Piazzale Aldo Moro, 5, 00185, Roma, Italy
[c] European Laboratory for Non-Linear Spectroscopy (LENS), via Nello Carrara 1, 50019, Sesto Fiorentino (FI), Italy
[d] National Research Council-National Institute of Optics (CNR-INO), Largo Fermi 6, 50125, Florence, Italy
[e] Univ. Grenoble Alpes, CEA, CNRS, Institut de Biologie Structurale, F-38044, Grenoble, France
[f] Elettra - Sincrotrone Trieste S.C.p.A, s.s. 14 km 163, 500 in Area Science Park, 34149, Trieste, Italy
[g] CNR-IOM – Istituto Officina dei Materiali, Via Alessandro Pascoli, 06123, Perugia, Italy

## HIGHLIGHTS

- Multi-technique approach was newly adopted to gain a deeper understanding of the molecular interaction mechanisms that underlie the binding of a human telomeric G-quadruplex and BRACO19.
- The essential role of the quadruplex conformation in its interaction with BRACO19 was elucidated. The unbound Tel22 adopts different conformations in $K^+$ or $Na^+$ environment.
- A multi-step binding process is confirmed to occur in both environments.
- In $K^+$ the interaction between the human telomeric G-quadruplex and BRACO19 involves the stacking mode, promoting moderate Tel22 dimerization.

## GRAPHICAL ABSTRACT

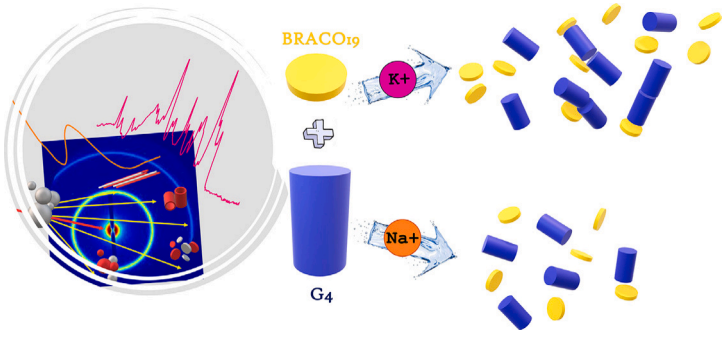


## ARTICLE INFO

*Keywords:*
G-quadruplex
BRACO19
Circular dichroism spectroscopy
Fluorescence spectroscopy
UV-visible absorption spectroscopy
UV resonant Raman spectroscopy

## ABSTRACT

Human telomeres (HTs) can form DNA G-quadruplex (G4), an attractive target for anticancer and antiviral drugs. HT-G4s exhibit inherent structural polymorphism, posing challenges for understanding their specific recognition by ligands. Here, we aim to explore the impact of different topologies within a small segment of the HT (Tel22) on its interaction with BRACO19, a rationally designed G4 ligand with high quadruplex affinity, already employed in *in-vivo* treatments. Our multi-technique approach is based on the combined use of a set of contactless spectroscopic tools. Circular dichroism and UV resonance Raman spectroscopy probe ligand-induced conformational changes in the G4 sequence, while UV-visible absorption, coupled with steady-state fluorescence spectroscopy, provides further insights into the electronic features of the complex, exploiting the photoresponsive properties of BRACO19. Overall, we find that modifying the topology of the unbound Tel22 through cations ($K^+$ or $Na^+$), serves as a critical determinant for ligand interactions and binding modes, thus

* Corresponding author.
*E-mail addresses:* valeria.libera@unipg.it (V. Libera), comez@iom.cnr.it (L. Comez).
[1] Equal contribution.
[2] Present address: Department of Life and Environmental Sciences, Marche Polytechnic University, via Brecce Bianche, 60131, Ancona, Italy.

https://doi.org/10.1016/j.saa.2024.124684
Received 18 April 2024; Received in revised form 12 June 2024; Accepted 18 June 2024
Available online 26 June 2024

influencing the HT-G4's assembly capabilities. Furthermore, we show how fluorescence serves as a valuable probe for recognizing cation-driven multimeric structures, which may be present in living organisms, giving rise to pathological forms.

## 1. Introduction

G-quadruplexes (G4s), unique secondary structures formed by guanine-rich nucleic acid sequences [1,2], have garnered significant attention for their pivotal roles in regulating gene expression, DNA replication, and genomic stability. G4s form four-stranded helical structures comprising several stacked flat arrays of four guanine bases connected through cyclic Hoogsteen hydrogen bonds, referred to as G-tetrads [3]. Three main classes of G4 topologies, differing in the orientation of the four guanine runs and the arrangement of the loop regions, are typically identified: parallel, antiparallel, and hybrid [4–6]. Their shape is influenced not only by the specific oligonucleotide sequence but also by environmental factors such as the type and concentration of ions, molecular density, and dehydration conditions [7–10]. G4s have been identified in telomeric regions, promoter sequences, and other critical genomic regions [11,12], displaying a wide variety of secondary structure conformations. The structural stability and the biological activity of G4 sequences have become the focus of extensive biochemical and pharmacological research. The principal aim is to develop ligands with a high degree of G4 targeting selectivity compared to canonical DNA.

Regarding the human telomeric (HT) sequences, considerable efforts have been devoted to exploring the influence of different environments [13–15] on the interaction with small ligands [16,17]. Research in this field proposes HT-G4 structures as appealing pharmacological targets [18] to inhibit telomerase activity in cancer cells [3,19]. Remarkably, some HT-G4 ligands are already undergoing medical trials [20,21]. However, the picture is complicated due to the high polymorphism of HT-G4 structures. Indeed, *in vivo* studies [22] revealed that HT-G4 structures tend to mainly assume a mixture of hybrid topologies.

In this framework, our work aims to explore the role of the HT-G4 topology in the interaction between a HT sequence and a model drug. Therefore, we chose the HT $AG_3(TTAG_3)_3$ (Tel22) sequence, which is capable of mimicking the HT-G4 secondary structure arrangements actually found in *in-vivo* [22], especially in potassium environment [23]. To further explore the distinct behavior of HT-G4s in mixtures of topologies compared to those adopting an almost unique conformation, we employed the same sequence in a $Na^+$ buffer. In this buffer, Tel22 predominantly adopts an antiparallel secondary structure [24]. Among all the available HT-G4 ligands, our study focuses on BRACO19, which has emerged as a highly promising rationally designed drug for potential therapeutic application. This compound has demonstrated remarkable potential in cancer therapy, exhibiting substantial growth inhibition in various cancer cell lines such as human uterus carcinoma UXF1138L [25], breast cancer [26], and glioblastoma multiforme [27]. Beyond its anticancer prowess, BRACO19 showcases additional versatility by demonstrating antiviral properties against HIV-1 and HSV-2 [28,29].

Even though BRACO19 is a well-studied ligand for HT-G4 structures [16,25,30], there is no clear information on its interaction with the HT-G4 under physiological conditions. This lack might originate from the polymorphism in HT-G4, which enables diverse binding modes with small molecules. Computational methods have shown that, when interacting with BRACO19, significant variations in the energetic stability of top/bottom stacking, intercalation, and groove binding modes can be observed depending on the initial conformation of the telomeric structure [16].

Therefore, gaining insight into these binding (or multi-binding) patterns represents a fundamental starting point for designing new promising drugs with enhanced performances [31,32].

Here, we propose an all-optical experimental strategy to probe the role and consequences of HT-G4 topologies in the interaction with drug molecules. Our focus is on the Tel22-BRACO19 binding under different buffer conditions. It is important to emphasize that the proposed approach can be extended to many other ligands, such as those, like BRACO19, that are photoresponsive. This peculiar property enables us to characterize binding affinity through ultraviolet–visible (UV–Vis) absorption titration and to explore the binding mode as well as potential charge rearrangements in the complex through fluorescence spectroscopy [33,34].

Furthermore, the combination of circular dichroism (CD) and UV resonance Raman (UVRR) spectroscopy provides information about the variations in secondary structure and molecular vibrations upon ligand binding [35–39]. The exceptional sensitivity of UVRR scattering, in comparison to conventional Raman spectroscopy, enables us to conduct experiments in highly diluted physiological conditions, but maintaining a satisfactory signal to noise ratio. Given that the structure of polymorphic HT-G4 sequences is significantly influenced by concentration, it is crucial to ensure the uniformity of all experiments for a comprehensive perspective. The synergy between the used techniques constitutes a key strength of the present investigation, allowing, in general, for a thorough exploration of the molecular interaction mechanisms between G4 and drugs.

## 2. Material and methods

### 2.1. Sample preparation

The oligonucleotide sequence $AG_3(TTAG_3)_3$ (Tel22) was purchased from Eurogentec (Belgium) and used without further purification. The DNA powder was dissolved in two buffers (50 mM K-phosphate buffer at pH 7, 0.3 mM EDTA, 150 mM KCl and 50 mM Na-phosphate buffer at pH 7, 0.3 mM EDTA, 150 mM NaCl) reaching 1 mM DNA concentration. The two solutions were heated to 95 °C for 5 min and then slowly cooled down to room temperature in ~3.5 h, and left at room temperature overnight. BRACO19 was purchased from Merck KGaA (Darmstadt, Germany) and used without other purification.

### 2.2. UV–Vis absorption spectroscopy

Absorption spectra were measured by Jasco V-570 spectrophotometer with a 1 mm path-length quartz cuvette. Spectra were recorded in the 200–500 nm range at room temperature. Absorption titration measurements were carried out using different stock solutions with fixed BRACO19 concentration (80 μM) and increasing the Tel22 concentration from 0 μM to 100 μM. Beside BRACO19 alone (Tel22 equal to 0 μM), those concentrations correspond to the following molar ratios for Tel22:BRACO29 complexes: 1:80, 1:40, 1:20, 1:10, 1:5, 1:3.3, 1:2.5, 1:2, 1:1.3, 1:1, 1:0.8. The titration was terminated when the wavelength and intensity of the absorption band of BRACO19 at about 363–373 nm did not change upon increasing the Tel22 concentration.

### 2.3. Fluorescence spectroscopy

Fluorescence experiments were carried out on the same samples prepared for absorption measurements, by exciting the samples with the 365 nm pulses of an Ekspla NT340 laser (repetition rate 10 Hz, 5 ns pulse duration). The laser power was kept below 5 mW. Photobleaching effects are minimized by the reduced size of the scattering volume (about 10 μm in size) as compared to the total solution. Samples were held in a suprasil quartz cuvette. The fluorescence emission was

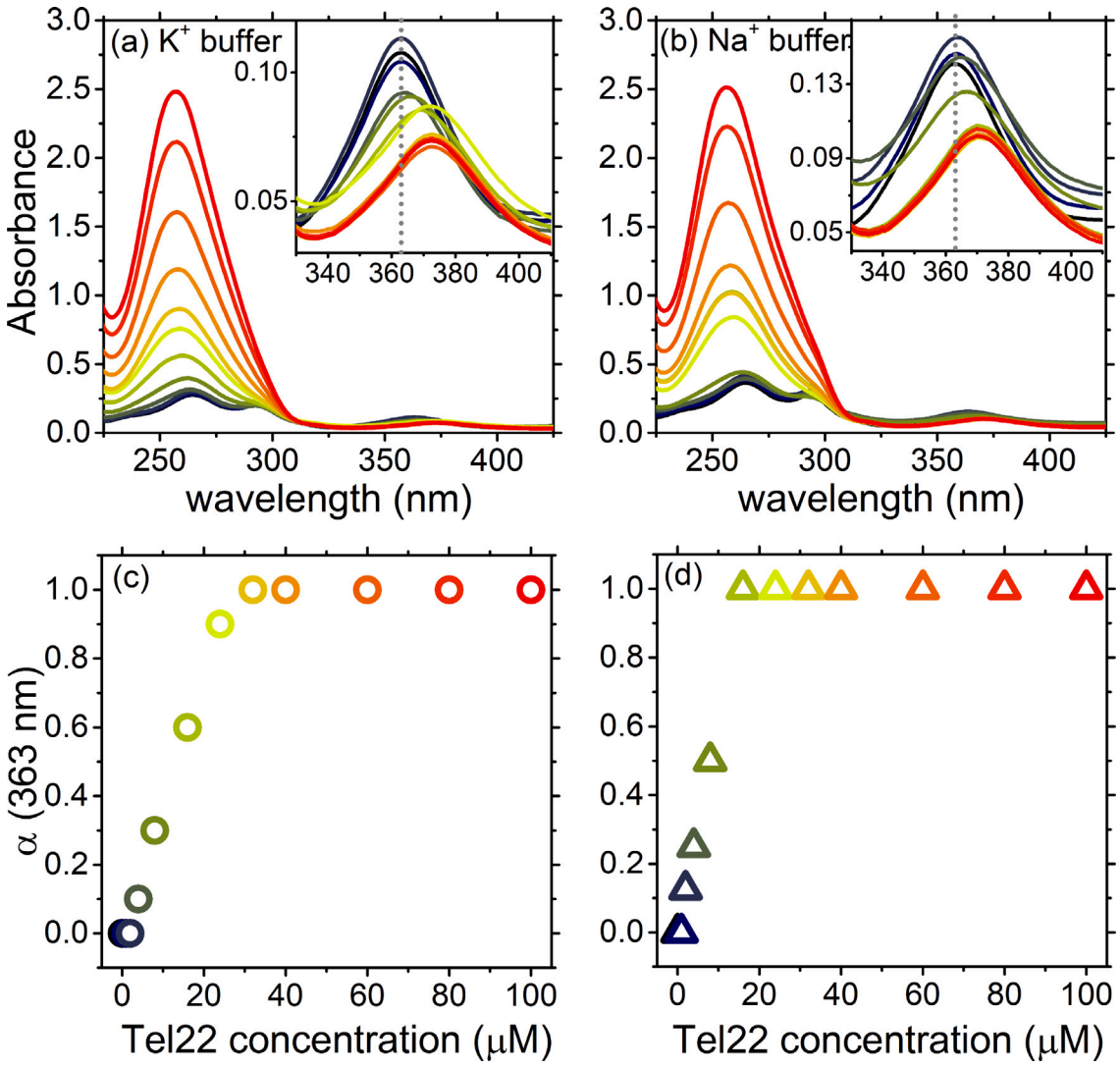


**Fig. 1.** UV–Vis absorption spectra of Tel22-BRACO19 complexes at fixed BRACO19 concentration (80 μM) and increasing Tel22 concentration from 0 to 100 μM: (a) in potassium and (b) in sodium environment. Dotted lines in the inset represent the maximum absorbance at 363 nm of the free BRACO19. Fraction of bound BRACO19 as a function of Tel22 concentration (c) in potassium and (d) in sodium environment, respectively.

collected at an angle of 90° with respect to the excitation beam with appropriate optics and delivered to a f = 3.2 Czerny Turner spectrograph (Horiba Ltd) equipped with a 600 gr/mm diffraction grating, ensuring a spectral resolution better than 1 nm. The dispersed fluorescence light was detected by a CCD. The spectra were processed and analyzed using LabSpec 6 and Origin 9 softwares.

### 2.4. Circular dichroism

CD experiments were carried out with Jasco J-810 spectropolarimeter. Since CD is very sensitive to quadruplex conformational changes, measurements were performed on the Tel22 alone at 30 μM concentration and on the complexed sample in stoichiometric ratios of Tel22:BRACO19 1:1, 1:2, and 1:4. To achieve the best signal-to-noise ratio, a 1 mm path-length quartz cuvette was utilized. Each spectrum was collected in the range from 220 to 350 nm, with a scan speed of 50 nm/min.

### 2.5. UV resonance Raman spectroscopy

UVRR measurements were performed at the IUVS beamline at Elettra Sincrotrone Trieste using a synchrotron-based set up [40], on the same samples measured through CD spectroscopy. A 10 mm path-length quartz cuvette was used as sample holder. The excitation wavelength was set at 250 nm by regulating the undulator gap aperture and monochromatizing the incoming radiation through a 750 cm focal length spectrograph equipped with holographic gratings at 1800 and 3600 groves/mm (Princeton Instruments). The Raman signal was collected in backscattering geometry and analyzed via a single-pass Czerny–Turner spectrometer (Princeton Instruments, 750 mm of focal length), equipped with holographic grating at 1800 g/mm, and detected using a UV-optimized CCD camera (resolution of about 2 cm-1/pixel). The calibration of the spectrometer was performed using cyclohexane (spectroscopic grade, Sigma-Aldrich). Beam power measured on the samples was about 4 μW.

## 3. Results and discussion

### 3.1. Tel22-BRACO19 titration experiments

To explore the influence of the cationic environment on the binding mechanisms of Tel22-BRACO19, we carried out a series of titration experiments through different steady-state optical spectroscopies. UV–Vis absorption and fluorescence measurements were performed to investigate the variations in the electronic properties of BRACO19 resulting

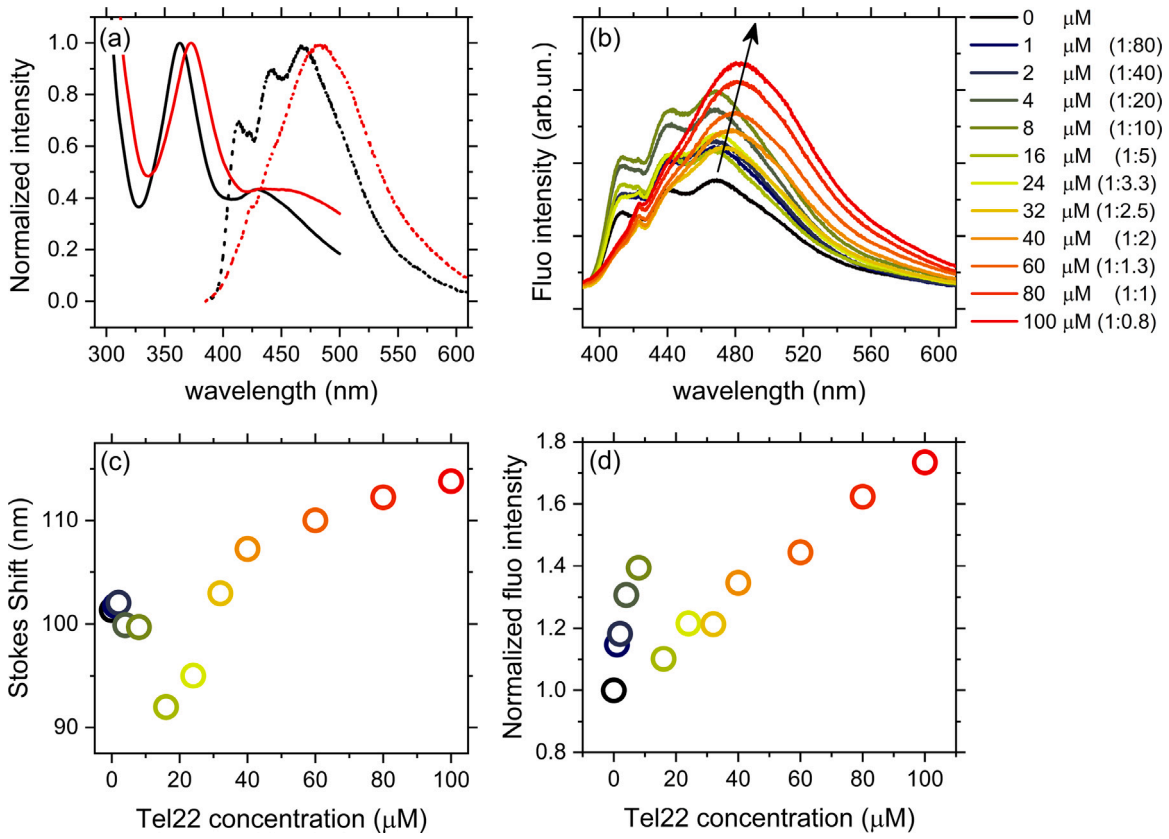


**Fig. 2.** Fluorescence results in potassium environment: (a) normalized absorbance (solid line) and fluorescence (dashed line) spectra of BRACO19 at 80 μM (black) and BRACO19-Tel22 complex at 100 μM of Tel22 (red), using a $\lambda$ = 365 nm excitation wavelength; (b) fluorescence spectra of Tel22-BRACO19 complex as a function of Tel22 concentration from 0 to 100 μM. (c) Stokes shift (defined in the text) and (d) intensity of fluorescence spectra at 490 nm as a function of Tel22 concentration.

from its interaction with Tel22. Figs. 1a and 1b report UV–Vis absorption spectra of BRACO19 at a fixed concentration (80 μM) as a function of Tel22 concentration from 0 to 100 μM. The corresponding values in terms of Tel22-BRACO19 stoichiometric ratios are reported in the Material and methods section. BRACO19 has characteristic absorption bands with three major peaks at 264 nm, 293 nm, and 363 nm. These bands are peculiar of aminoacridine structures and result from $\pi - \pi^*$ electronic transitions of acridine rings [41]. Since Tel22 has an absorption band at ~260 nm and a free spectral window at higher wavelengths, the evolution of the band centered at 363 nm was mainly considered in the titration spectra (see the inset of Figs. 1a and 1b). The changes in this band, indeed, more prominently reflect the interaction between Tel22 and BRACO19, making it an effective spectroscopic descriptor for the formation of the complex and for the monitoring of binding mechanisms.

In $K^+$ environment, upon increasing the Tel22 concentration, the BRACO19 absorption band at 363 nm red-shifts of 10 nm (bathochromic effect) and decreases of ~60% (hypocromic effect, see Fig. S1a of Supporting Information). In $Na^+$ environment, the BRACO19 band is affected by a lower red-shift (~8 nm) and the absorbance titration trend shows a two-step behavior. Indeed, the absorption slightly increases for Tel22 concentration up to 8 μM (i.e. Tel22:BRACO19 1:10) and then decreases of ~35% for higher HT-G4 concentrations, as shown in Fig. S1b of Supporting Information. According to previous literature [42–44], absorption bands of ligands that, due to the interaction with DNA, exhibit a red-shift greater than 15 nm and a hypochromic effect larger than 35% are indicative of an intercalative binding mechanism. Instead, when the red-shift is more than 10 nm, the interaction is likely due to $\pi$-stacking [45]. Based on our spectral trends, it is highly plausible that BRACO19 and Tel22 interact via stacking modes in $K^+$ environment. In contrast, in $Na^+$ buffer, the lower red-shift indicates a different type of interaction, possibly involving groove-loop bindings.

Furthermore, in both environments, a clear isosbestic point cannot be identified during the titration. This evidence represents an indication that the Tel22-BRACO19 binding process cannot be related to a two-state interaction mechanism, which involves the free and the bound states only. The present data support then a multi-step binding mechanism, consistent with previous findings from surface plasmon resonance and calorimetry, where two steps were found, the first binding mode being approximately ten times more efficient than the second [46].

To obtain information on the saturation binding curve, the fraction of bound BRACO19 as a function of Tel22 concentration is shown in Fig. 1c and Fig. 1d. The concentrations of bound ($C_b$) and free ($C_f$) BRACO19 were evaluated by using the relations $C_f = C \cdot (1 - \alpha)$ and $C_b = C - C_f$. Here, C is the total ligand concentration (80 μM) and $\alpha$ is calculated through the equation: $\alpha = (A_f - A)/(A_f - A_b)$, where $A_f$ and $A_b$ are the absorbances of the free and fully bound BRACO19 at 363 nm respectively, and A is the absorbance at the same wavelength for each measurement. In $K^+$ environment, the bound fraction reaches a plateau at a DNA:ligand stoichiometric ratio of about 1:2.5, while in $Na^+$ buffer the plateau is obtained at a higher stoichiometric ratio (1:4).

The interaction of BRACO19 with Tel22 was further studied using fluorescence spectroscopy. The ligand fluorescence, obtained by exciting the sample in solution with a 365 nm wavelength, depends on both the molecular structure and the environment around the molecule. A broad fluorescence band centered at ~470 nm was observed in the presence of both cations, as reported in Figs. 2a and 3a. Comparing the absorption and the emission spectra of BRACO19 in $K^+$ and $Na^+$ (Fig. S2 of Supporting Information), we observed that changing the buffer solution led to a shift in the fluorescence wavelength, but not in the absorption one, indicating a stronger interaction between solvent and BRACO19 in the excited state. Indeed, when the shift of the emission band is higher than that of the absorption band, the molecule

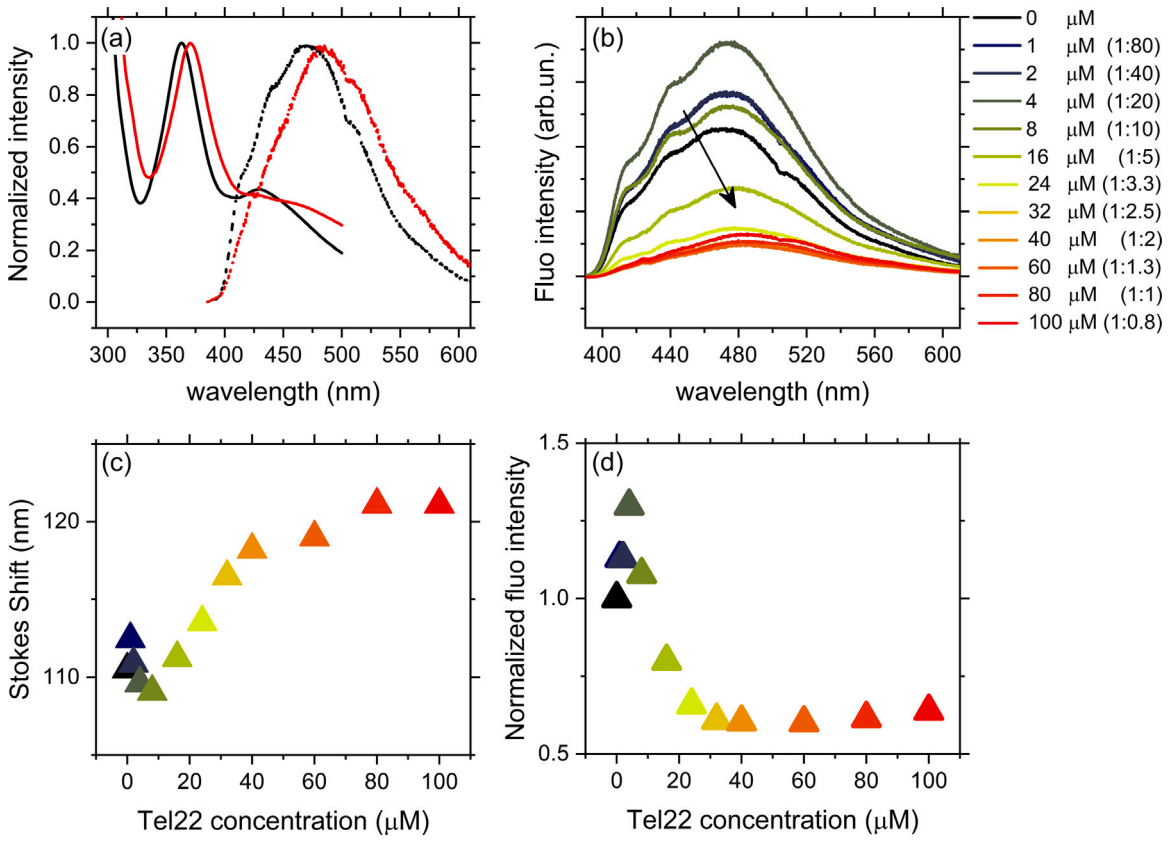


**Fig. 3.** Fluorescence results in sodium environment: (a) normalized absorbance (solid line) and fluorescence (dashed line) spectra of BRACO19 at 80 μM (black) and BRACO19-Tel22 complex at 100 μM of Tel22 (red), using a $\lambda$ = 365 nm excitation wavelength. (b) Fluorescence spectra of Tel22-BRACO19 complex as a function of Tel22 concentration from 0 μM to 100 μM. (c) Stokes shift (defined in the text) and (d) intensity of fluorescence spectra at 490 nm as a function of Tel22 concentration.

shows a greater dipole moment in the excited state than in the ground state [47]. Acridine-based molecules, such as BRACO19, exhibit an increase in dipole moment when transitioning from the ground to the excited state. In fact, the electronic charge distribution of the $\pi - \pi^*$ excited state is more extended than that of the ground state, making the former more polarizable [47].

Fig. 2b shows the fluorescence titration spectra of Tel22-BRACO19 complexes in $K^+$ buffer at the same concentrations used in the absorption experiments. Up to ~16 μM, corresponding to Tel22:BRACO19 1:5 molar ratio, the spectral shape does not change but its intensity increases. Above that point, the increase in HT-G4 concentration is related to a drastic change of the fluorescence signal, which results in a structureless, red-shifted, broad band. The Stokes shift, defined as the difference between the spectral position of the maximum of the emission band and the maximum of the absorption one, is reported in Fig. 2c as a function of Tel22 concentration, while the intensity of the spectra at 490 nm is shown in Fig. 2d. They both suggest the occurrence of a multi-step binding mechanism between Tel22 and BRACO19, as already pointed out by the absorption results.

It has been already observed in the literature that acridine molecules could form large aggregates in solution, resulting in a self-quenching of the fluorescence signal [48,49]. Therefore, in our case, the initial enhancement of fluorescence intensity upon Tel22 addition up to 16 μM could be attributed to the dissociation of ligand aggregates caused by the preferential interaction of BRACO19 with G4. Furthermore, this increase in fluorescence intensity is not accompanied by a change of the spectral shape, thus suggesting electrostatic interactions between the negatively charged Tel22 phosphate groups and the positively charged BRACO19 quaternary nitrogen [45]. Further, by increasing the Tel22 concentration, the shape, the position, and the intensity of the emission band of the complex has changed, thus indicating a variation of the Tel22-BRACO19 interaction. In particular, the red-shift of the spectral center of ~20 nm and the slight light-up prove that BRACO19 aromatic rings start to interact possibly through head-to-tail $\pi - \pi$ stacking.

Steady-state fluorescence titration measurements were also carried out in $Na^+$ aqueous solutions, as reported in Fig. 3. The evolution of the fluorescence spectrum of Tel22-BRACO19 complex upon increasing Tel22 concentration resulted in a fluorescence decrease with an almost complete quenching (see Fig. 3b). The efficient fluorescence quenching allows monitoring the complexation process. In the first part of the titration, the optical changes are qualitatively similar to those occurring in $K^+$ buffer. In this instance as well, BRACO19 may form aggregates in solution, which can be dissociated upon HT-G4 addition. Also in this case, the initial light-up of fluorescence intensity up to 8 μM HT-G4 concentration, without any differences in terms of position or shape, indicates an electrostatic interaction between BRACO19 and Tel22. This is in line with our expectations, considering the tricationic nature of the ligand, which may facilitate long-range interactions with the negatively charged phosphate groups along the HT-G4 grooves. Further increasing Tel22 concentration, an almost complete fluorescence quenching was observed. This evidence, along with the hypochromic red-shift of the absorption band during the titration (Fig. 3c and Fig. 3d), suggests that BRACO19 binds to the outside of the Tel22 molecule involving interactions that are not limited to the electrostatic forces [50].

### 3.2. Circular dichroism and UVRR spectroscopy

Modifications at the secondary structural level induced by BRACO19 on Tel22 were identified by examining the CD signal of the complexes. In $K^+$ environment, Tel22 has a characteristic CD profile of a mixture of conformations, with a maximum at ~290 nm, a shoulder at 270 nm, and a minimum at ~234 nm. The use of a specific algorithm, which was

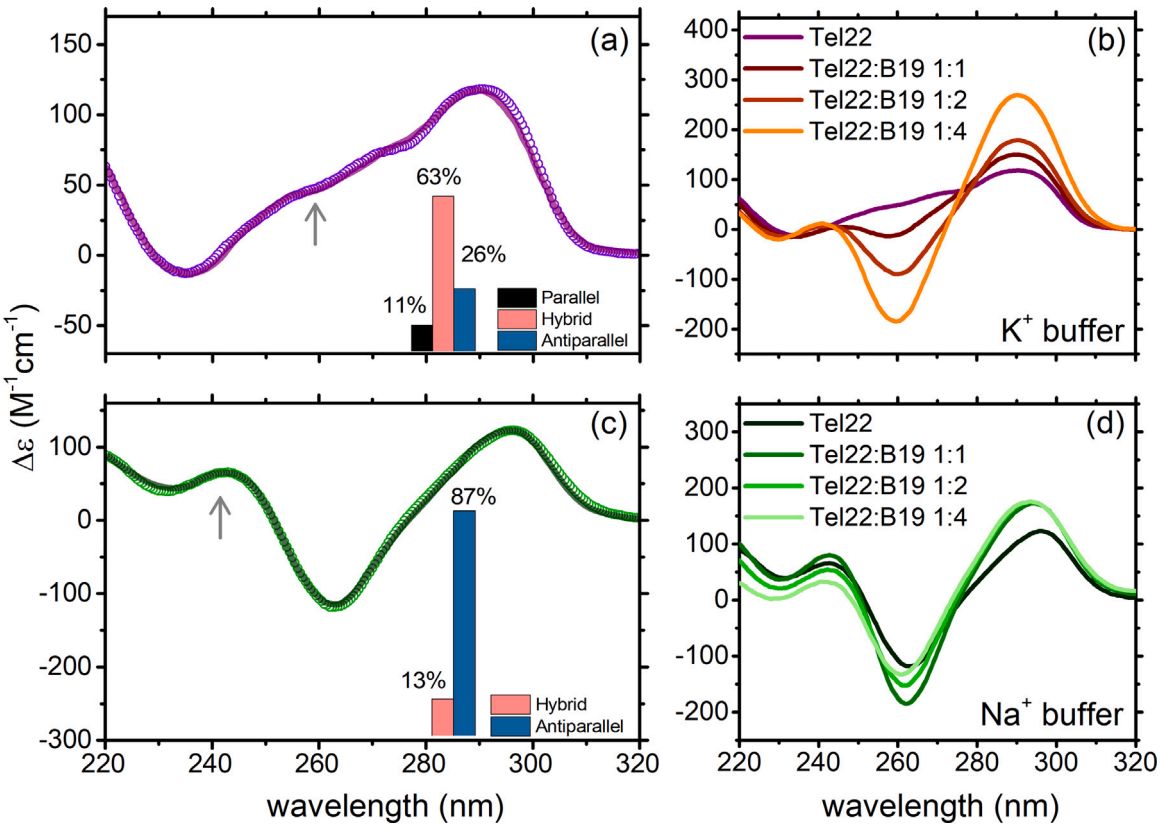


**Fig. 4.** CD spectra of Tel22 in (a) $K^+$ buffer and (c) $Na^+$ buffer, along with the best fits using the algorithm explained in the text [51]. The corresponding percentages of the tertiary structure components (parallel, antiparallel, and hybrid) are reported in the inset of both panels. CD spectra of Tel22 complexed with BRACO19 at four different molar ratios (1:0, 1:1, 1:2, and 1:4): (b) in potassium and (d) in sodium environment.

developed to derive the secondary structure content of quadruplexes from their experimental CD spectra [51], provided the percentages of the main different species. The two most prevalent topologies were the hybrid (~63%) and the antiparallel (~26%) ones, as represented in Fig. 4a (see also Table S1 in Supporting Information). Fig. 4b shows Tel22-BRACO19 in $K^+$ buffer at selected stoichiometric ratios, namely 1:0, 1:1, 1:2, and 1:4. The complexation with BRACO19 induces a drastic change of the CD features, with an increase of the peak at 290 nm, the formation of a maximum at 240 nm and a minimum at 260 nm. Therefore, upon complexation, the Tel22 structure undergoes conformational switching towards an increasingly antiparallel-like structure at the expense of the parallel population. This change is accompanied by an overall increase in the maximum and minimum intensities as the BRACO19 concentration increases.

Conversely, Tel22 in $Na^+$ adopts a predominantly antiparallel topology (~87%) with two maxima at ~296 nm and at 243 nm and a minimum at 263 nm (see Fig. 4c). Fig. 4d shows that, different from that in the $K^+$ environment, as the ligand concentration increases, the peak positions slightly shift towards shorter wavelengths upon complexation and their intensities slightly vary. This observation supports the interpretation of different interaction mechanisms of BRACO19 with Tel22 in the two investigated cationic environments.

To gain insights into the effects induced by complexation on the HT-G4 structure at a molecular level, UVRR spectroscopy was employed exploiting the 250 nm exciting wavelength. This wavelength is commonly chosen because it is near the Tel22 absorption maximum, thus ensuring a significant, selective amplification of the vibrational modes of quadruplex structure. In particular, the bands within the 1150–1600 $cm^{-1}$ range predominantly arise from the combination of vibrational motions associated with the exocyclic rings of the base residues. The UVRR spectra, measured for Tel22 and Tel22-BRACO19 samples at the same stoichiometric molar ratios employed for the CD experiments, are shown in Figs. 5a and 5c, in $K^+$ and in $Na^+$ environments, respectively, over the wavenumber range from 1200 to 1800 $cm^{-1}$.

This spectral range contains bands that are mostly ascribed to vibrations of dG residues, with minimal contributions from dA, which is less stoichiometrically significant in Tel22 [38,52–54]. Changes of the intensity and/or frequency shifts of these peaks can be associated with environmental, and thus conformational effects.

As the BRACO19 contribution strongly influences the UVRR signal above 1500 $cm^{-1}$ (see Fig. S3 of the Supporting Information) thus making data treatment challenging, we restricted our detailed analysis to lower wavenumber. All the spectra have been normalized on the OH stretching band at ~3400 $cm^{-1}$. By using Gaussian shape functions as reported in Refs. [35,37], it was possible to reproduce the vibrational features from 1280 to 1520 $cm^{-1}$. Representative best-fit curves are shown for the unbound samples in Figs. 5b and 5d. The bands that have proven to be particularly informative are those centered at 1323 and 1337 $cm^{-1}$, hereafter referred to as I and II, and that peaked at 1483 $cm^{-1}$, referred to as III. The I and II bands are indicators of glycosidic torsion angles of guanosines, respectively C2'-endo/syn-G and C2'-endo/anti-G [55]. Thus, the ratio between the corresponding areas, i.e. $A_I/A_{II}$, can be considered an identifier of the conformational change from an "hybrid-like" structure to a more antiparallel one: the higher the intensity of I, the higher the antiparallel population [56]. This ratio is reported in Fig. 6 as a function of the BRACO19 concentration.

It is evident that, in $K^+$ buffer, this parameter increases as a function of the Tel22:BRACO19 stoichiometric ratio, indicating a rise in the antiparallel population. Remarkably, a similar trend is observed in the behavior of the CD signal taken at a 260 nm wavelength (Fig. 6a), which is a marker for the parallel conformation, whose decrease is compensated by the corresponding growth of the antiparallel component. A

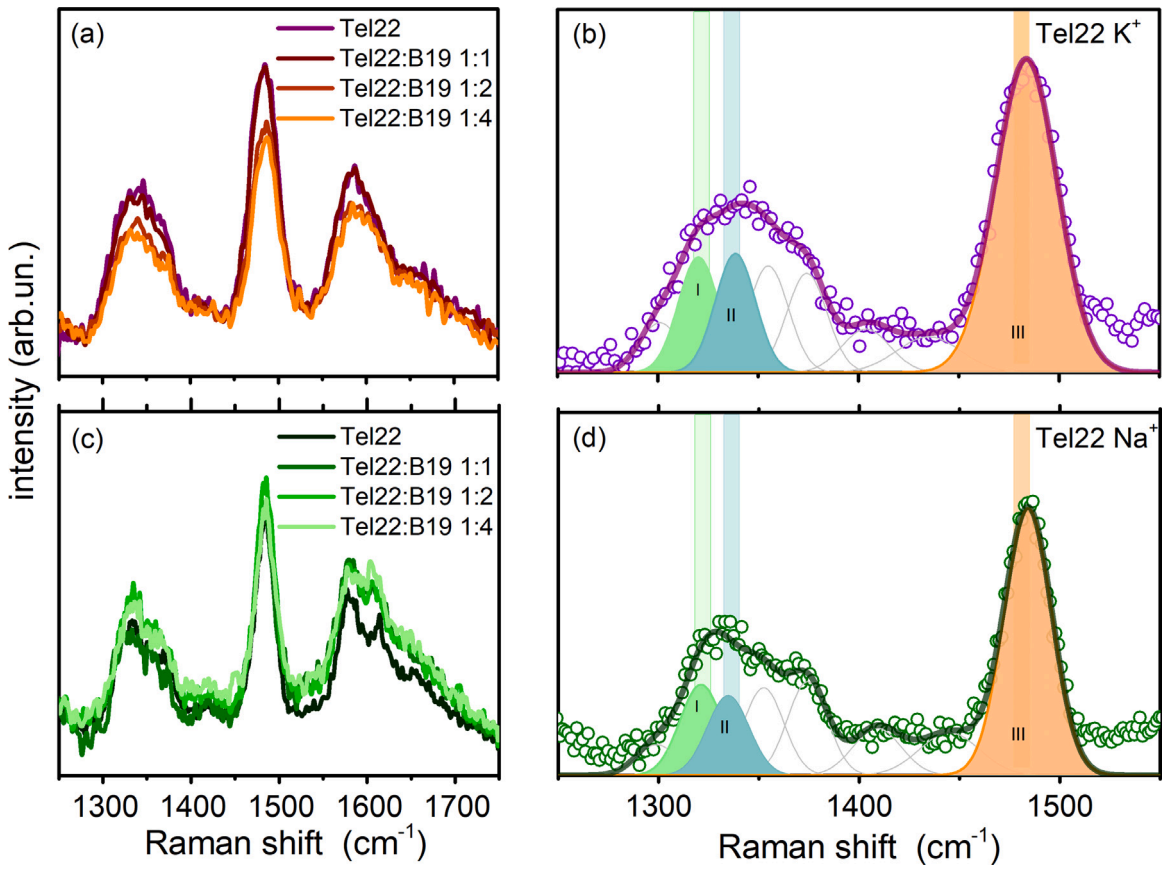


**Fig. 5.** UVRR spectra of Tel22 complexed with BRACO19 at four different molar ratios (1:0, 1:1, 1:2, and 1:4): (a) in potassium and (c) in sodium environment. UVRR spectra (circles) and the best fitting results (solid lines) of Tel22 in the two different environments: (b) $K^+$ buffer and (d) $Na^+$ buffer. The main representative vibrational bands are indicated with I (green), II (cyan), and III (orange). Gray lines represent the other components used for the deconvolution of the whole spectral region.

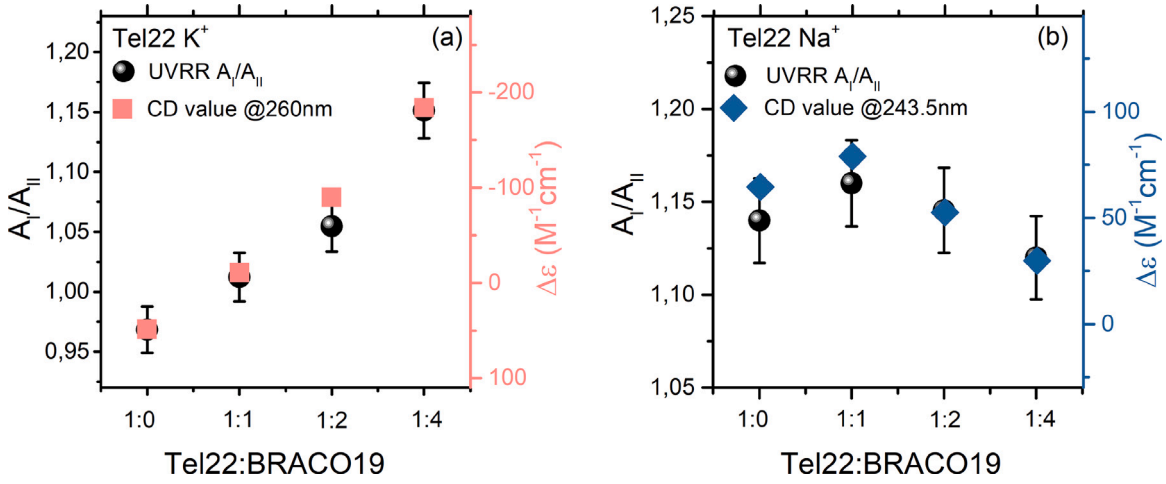


**Fig. 6.** (a) Intensity ratio of the UVRR bands indicated as I and II in Fig. 5 (black circles) compared to the CD intensity at 260 nm (pink squares) for the different Tel22-BRACO19 stoichiometric ratios in $K^+$ environment. (b) Analogous of panel (a) in $Na^+$ environment with blue symbols representing the CD intensity at 243.5 nm.

similar correlation between UVRR and CD can also be observed in the case of $Na^+$ environment. Here, the $A_I/A_{II}$ ratio does not significantly vary in all the analyzed samples, a behavior perfectly reproduced by the value of ellipticity at about 240 nm, which is indicative of the antiparallel population. Both of these parameters do not suggest remarkable alterations in the secondary structure, reinforcing the idea that BRACO19 exerts minimal influence on the Tel22 topology in the $Na^+$ environment.

Informative insights can be further obtained by examining band III, which arises from the bending of C8–H and the stretching of N9–C8 and C8–N7 [52,53]. A decrease in the Raman signal of this peak, i.e. the hypochromic effect, upon BRACO19 complexation was observed in $K^+$ environment (see Fig. S4 in Supporting Information) and can be ascribed to a modification of base stacking interactions, compatible with an end-stacking binding mode [38,54,57]. On the contrary, in $Na^+$ environment, no evident hypochromism was observed (see Fig. S4

in Supporting Information). These observations are consistent with the results obtained from UV–Vis absorption and fluorescence titrations.

It is worth noting that, when comparing the spectrum of Tel22 in $Na^+$ (whose topology is predominantly antiparallel) with that of the Tel22-BRACO19 1:4 complex in $K^+$ (Fig. S5a of Supporting Information), there is a notable overlap in the region of glycosidic bond markers, and both spectra show comparable $A_I/A_{II}$ ratio (see Fig. S5b of Supporting Information). This observation confirms the ability of the BRACO19 to induce conformational switching from a mixture of conformations (in hybrid prevalence) to an antiparallel-like topology in Tel22 in $K^+$ environment.

## 4. Conclusions

In this study, a multi-technique approach was newly adopted to gain a deeper understanding of the molecular interaction mechanisms that underlie the binding of Tel22, a highly polymorphic segment of the DNA telomere, and BRACO19, a model ligand selected for its potential application in cancer therapy and antiviral treatments.

By integrating structural and conformational information from CD and UVRR spectroscopy, along with electronic properties revealed by UV–Vis absorption and fluorescence spectroscopy, the essential role of the quadruplex conformation in its interaction with BRACO19 was elucidated. Indeed, the unbound Tel22 adopts different conformations in $K^+$ or $Na^+$ environment. Even though BRACO19 is capable to bind both topologies, we demonstrated that it induces a conformational switching only in $K^+$ buffer, where Tel22 is driven from a mixture of hybrid conformations towards a predominantly antiparallel secondary structure upon BRACO19 complexation. On the contrary, in $Na^+$ buffer, the prevalent Tel22 antiparallel topology does not significantly vary upon BRACO19 complexation. UV–Vis absorption and fluorescence results provide important information on the BRACO19 binding mode. A multi-step binding process is confirmed to occur in both environments. In $Na^+$ buffer, BRACO19 seems to adopt groove binding modes predominantly. Conversely, in a $K^+$ environment, UV–Vis absorption and UVRR measurements revealed that the interaction between Tel22 and BRACO19 involves the stacking mode, promoting moderate Tel22 dimerization. This observation, which aligns with recent suggestions derived from a combined analysis of structural experiments and coarse-grained simulations [58], is also supported by small-angle X-ray scattering (SAXS) experiments performed on the Tel22 complexes in $K^+$ buffer, at different DNA/ligand molar ratios (i.e. 1:1, 1:2, and 1:4). SAXS profiles of Tel22 samples with ligand show an excess scattering intensity for $Q < 1\ nm^{-1}$ compared to the plateau observed with Tel22 monomers (see Fig. S6), signaling the presence of G4 aggregates for stoichiometric ratios higher than 1:2. The emergence of multimers is further validated by our fluorescence results, which suggest the possible formation of J-type aggregates, with monomers aligned head-to-tail [59,60]. Indeed, the bathochromic effect along with the light-up of the fluorescence emission band could be attributed to the creation of strongly coupled multimers, as recently reported in the literature for pseudoisocyanine dyes and DNA duplex [61].

In conclusion, we provided evidence that the Tel22 topology, here selected by the cationic environment, serves as a critical determinant for ligand interactions and binding modes, influencing also the stacking capability of the quadruples. Interestingly, Tel22-BRACO19 complexes in a $K^+$ environment are found to be more prone to form multimeric structures than in $Na^+$ solution. This result arises by the application of fluorescence to G4-based systems, which helps to identify the type of aggregates. The method applied here, in combination with structural and computational techniques [58], could provide a promising multi-messenger investigative approach for a more rationalized design of specific molecules capable of binding to flexible HT DNA [62–66]. Given the relevance of multimeric G4s as potentially exerting deleterious effects in the pathogenic cascade of various diseases [62], the efforts to assess the affinity of new ligands for multimeric HT-G4s hold the potential for significant impact across various fields, including medicine, biotechnology, and pharmacology.

## Funding

This work has been funded by the European Union – NextGenerationEU under the Italian Ministry of University and Research (MUR) National Innovation Ecosystem grant ECS00000041 - VITALITY - CUP B43C22000470005 and J97G22000170005. V.L., A.P., L.C. acknowledge Università degli Studi di Perugia and MUR for support within the project Vitality. V.L., C.F., F.R. and C.P. received support from the project Scientific Data and Computing "CarESS" (Università di Perugia, D.R. n. 597). The authors also thank the ESRF for providing beamtime allocation (proposal MX-2586).

## CRediT authorship contribution statement

**Valeria Libera:** Writing – review & editing, Writing – original draft, Visualization, Validation, Methodology, Investigation, Formal analysis, Data curation, Conceptualization. **Claudia Fasolato:** Writing – review & editing, Writing – original draft, Visualization, Validation, Methodology, Investigation, Formal analysis, Data curation. **Francesca Ripanti:** Writing – review & editing, Writing – original draft, Visualization, Formal analysis, Data curation. **Sara Catalini:** Writing – review & editing, Writing – original draft, Visualization, Formal analysis, Data curation. **Luca Bertini:** Writing – review & editing, Visualization, Validation. **Caterina Petrillo:** Writing – review & editing, Methodology, Funding acquisition. **Giorgio Schirò:** Investigation, Writing – review & editing. **Francesco D'Amico:** Writing – review & editing, Investigation, Data curation. **Barbara Rossi:** Writing – review & editing, Investigation, Data curation. **Alessandro Paciaroni:** Writing – review & editing, Supervision, Funding acquisition, Conceptualization. **Lucia Comez:** Writing – review & editing, Writing – original draft, Visualization, Validation, Supervision, Methodology, Investigation, Funding acquisition, Formal analysis, Data curation, Conceptualization.

## Declaration of competing interest

The authors declare that they have no known competing financial interests or personal relationships that could have appeared to influence the work reported in this paper.

## Data availability

Data will be made available on request.

## Acknowledgments

The authors acknowledge Elettra Sincrotrone Trieste for providing access to its synchrotron radiation facilities and for financial support (proposal numbers 20200281 and 20190362). The BL10.2-IUVS beamline scientists are also acknowledged for their kind support during the Raman measurements, and A. Gessini for several technical discussions. We are finally very grateful to J.B. Chaires and J.O. Trent for providing the script to analyze CD spectra.

## Appendix A. Supplementary data

Supplementary material related to this article can be found online at https://doi.org/10.1016/j.saa.2024.124684.

## References

[1] S. Burge, G.N. Parkinson, P. Hazel, A.K. Todd, S. Neidle, Quadruplex DNA: sequence, topology and structure, Nucl. Acids Res. 34 (19) (2006) 5402–5415.
[2] M.L. Bochman, K. Paeschke, V.A. Zakian, DNA secondary structures: stability and function of G-quadruplex structures, Nature Rev. Genet. 13 (11) (2012) 770–780.
[3] S. Neidle, Quadruplex nucleic acids as targets for anticancer therapeutics, Nat. Rev. Chem. 1 (5) (2017) 0041.

[4] A.I. Karsisiotis, N.M. Hessari, E. Novellino, G.P. Spada, A. Randazzo, M. Webba da Silva, Topological characterization of nucleic acid G-quadruplexes by UV absorption and circular dichroism, Angew. Chem. Int. Ed. 50 (45) (2011) 10645–10648.
[5] M. Webba da Silva, Geometric formalism for DNA quadruplex folding, Chem. Eur. J. 13 (35) (2007) 9738–9745.
[6] S. Neidle, G.N. Parkinson, The structure of telomeric DNA, Curr. Opin. Struct. Biol. 13 (3) (2003) 275–283.
[7] J.L. Huppert, Structure, location and interactions of G-quadruplexes, FEBS J. 277 (17) (2010) 3452–3458.
[8] A.T. Phan, V. Kuryavyi, D.J. Patel, DNA architecture: from G to Z, Curr. Opin. Struct. Biol. 16 (3) (2006) 288–298.
[9] N. Smargiasso, F. Rosu, W. Hsia, P. Colson, E.S. Baker, M.T. Bowers, E. De Pauw, V. Gabelica, G-quadruplex DNA assemblies: loop length, cation identity, and multimer formation, J. Am. Chem. Soc. 130 (31) (2008) 10208–10216.
[10] B. Heddi, A.T. Phan, Structure of human telomeric DNA in crowded solution, J. Am. Chem. Soc. 133 (25) (2011) 9824–9833.
[11] R. Hänsel-Hertsch, M. Di Antonio, S. Balasubramanian, DNA G-quadruplexes in the human genome: detection, functions and therapeutic potential, Nat. Rev. Mol. Cell Biol. 18 (5) (2017) 279–284.
[12] J.L. Huppert, S. Balasubramanian, Prevalence of quadruplexes in the human genome, Nucl. Acids Res. 33 (9) (2005) 2908–2916.
[13] V. Libera, F. Ripanti, C. Petrillo, F. Sacchetti, J. Ramos-Soriano, M.C. Galan, G. Schirò, A. Paciaroni, L. Comez, Stability of human telomeric G-quadruplexes complexed with photosensitive ligands and irradiated with visible light, Int. J. Mol. Sci. 24 (10) (2023) 9090.
[14] D. Bhattacharyya, G. Mirihana Arachchilage, S. Basu, Metal cations in G-quadruplex folding and stability, Front. Chem. 4 (2016) 38.
[15] J. Jana, K. Weisz, Thermodynamic stability of G-quadruplexes: Impact of sequence and environment, ChemBioChem 22 (19) (2021) 2848–2856.
[16] B. Machireddy, H.-J. Sullivan, C. Wu, Binding of BRACO-19 to a telomeric G-quadruplex DNA probed by all-atom molecular dynamics simulations with explicit solvent, Molecules 24 (6) (2019) 1010.
[17] M.P. O'Hagan, J. Ramos-Soriano, S. Haldar, S. Sheikh, J.C. Morales, A.J. Mulholland, M.C. Galan, Visible-light photoswitching of ligand binding mode suggests G-quadruplex DNA as a target for photopharmacology, Chem. Commun. 56 (38) (2020) 5186–5189.
[18] G.W. Collie, G.N. Parkinson, The application of DNA and RNA G-quadruplexes to therapeutic medicines, Chem. Soc. Rev. 40 (12) (2011) 5867–5892.
[19] D. Sun, B. Thompson, B.E. Cathers, M. Salazar, S.M. Kerwin, J.O. Trent, T.C. Jenkins, S. Neidle, L.H. Hurley, Inhibition of human telomerase by a G-quadruplex-interactive compound, J. Med. Chem. 40 (14) (1997) 2113–2116.
[20] J.E. Rosenberg, R.M. Bambury, E.M. Van Allen, H.A. Drabkin, P.N. Lara, A.L. Harzstark, N. Wagle, R.A. Figlin, G.W. Smith, L.A. Garraway, et al., A phase II trial of AS1411 (a novel nucleolin-targeted DNA aptamer) in metastatic renal cell carcinoma, Invest. New Drugs 32 (2014) 178–187.
[21] H. Xu, L.H. Hurley, A first-in-class clinical G-quadruplex-targeting drug. The bench-to-bedside translation of the fluoroquinolone QQ58 to CX-5461 (Pidnarulex), Bioorg. & Med. Chem. Lett. (2022) 129016.
[22] G. Biffi, D. Tannahill, J. McCafferty, S. Balasubramanian, Quantitative visualization of DNA G-quadruplex structures in human cells, Nat. Chem. 5 (3) (2013) 182–186.
[23] A. Ambrus, D. Chen, J. Dai, T. Bialis, R.A. Jones, D. Yang, Human telomeric sequence forms a hybrid-type intramolecular G-quadruplex structure with mixed parallel/antiparallel strands in potassium solution, Nucl. Acids Res. 34 (9) (2006) 2723–2735.
[24] Y. Wang, D.J. Patel, Solution structure of the human telomeric repeat d [AG3 (T2AG3) 3] G-tetraplex, Structure 1 (4) (1993) 263–282.
[25] A.M. Burger, F. Dai, C.M. Schultes, A.P. Reszka, M.J. Moore, J.A. Double, S. Neidle, The G-quadruplex-interactive molecule BRACO-19 inhibits tumor growth, consistent with telomere targeting and interference with telomerase function, Cancer Res. 65 (4) (2005) 1489–1496.
[26] S. Di Somma, J. Amato, N. Iaccarino, B. Pagano, A. Randazzo, G. Portella, A.M. Malfitano, G-Quadruplex binders induce immunogenic cell death markers in aggressive breast cancer cells, Cancers 11 (11) (2019) 1797.
[27] M. Gunaratnam, O. Greciano, C. Martins, A.P. Reszka, C.M. Schultes, H. Morjani, J.-F. Riou, S. Neidle, Mechanism of acridine-based telomerase inhibition and telomere shortening, Biochem. Pharmacol. 74 (5) (2007) 679–689.
[28] E. Ruggiero, S.N. Richter, Viral G-quadruplexes: New frontiers in virus pathogenesis and antiviral therapy, in: Annual Reports in Medicinal Chemistry, Vol. 54, Elsevier, 2020, pp. 101–131.
[29] S. Artusi, M. Nadai, R. Perrone, M.A. Biasolo, G. Palu, L. Flamand, A. Calistri, S.N. Richter, The Herpes Simplex Virus-1 genome contains multiple clusters of repeated G-quadruplex: Implications for the antiviral activity of a G-quadruplex ligand, Antiviral Res. 118 (2015) 123–131.
[30] B. Pagano, N. Iaccarino, A. Di Porzio, A. Randazzo, J. Amato, Screening of DNA G-quadruplex stabilizing ligands by nano differential scanning fluorimetry, Analyst 144 (22) (2019) 6512–6516.
[31] A. Lauria, A. Terenzi, R. Bartolotta, R. Bonsignore, U. Perricone, M. Tutone, A. Martorana, G. Barone, A. Maria Almerico, Does ligand symmetry play a role in the stabilization of DNA G-quadruplex host-guest complexes? Curr. Med. Chem. 21 (23) (2014) 2665–2690.
[32] S.A. Ohnmacht, S. Neidle, Small-molecule quadruplex-targeted drug discovery, Bioorg. Med. Chem. Lett. 24 (12) (2014) 2602–2612.
[33] A. Roy, D. Basu, D. Bose, A. Dutta, S.G. Dastidar, S. Chatterjee, Identification and characterization of a flexile G-quadruplex in the distal promoter region of stemness gene REX1, Int. J. Biol. Macromol. 231 (2023) 123263.
[34] C. Wei, G. Jia, J. Yuan, Z. Feng, C. Li, A spectroscopic study on the interactions of porphyrin with G-quadruplex DNAs, Biochemistry 45 (21) (2006) 6681–6691.
[35] V. Libera, F. Bianchi, B. Rossi, F. D'Amico, C. Masciovecchio, C. Petrillo, F. Sacchetti, A. Paciaroni, L. Comez, Solvent vibrations as a proxy of the telomere G-quadruplex rearrangements across thermal unfolding, Int. J. Mol. Sci. 23 (9) (2022) 5123.
[36] J. Amato, N. Iaccarino, F. D'Aria, F. D'Amico, A. Randazzo, C. Giancola, A. Cesàro, S. Di Fonzo, B. Pagano, Conformational plasticity of DNA secondary structures: Probing the conversion between i-motif and hairpin species by circular dichroism and ultraviolet resonance Raman spectroscopies, Phys. Chem. Chem. Phys. 24 (11) (2022) 7028–7044.
[37] S. Di Fonzo, J. Amato, F. D'Aria, M. Caterino, F. D'Amico, A. Gessini, J.W. Brady, A. Cesàro, B. Pagano, C. Giancola, Ligand binding to G-quadruplex DNA: New insights from ultraviolet resonance Raman spectroscopy, Phys. Chem. Chem. Phys. 22 (15) (2020) 8128–8140.
[38] F. Bianchi, L. Comez, R. Biehl, F. D'Amico, A. Gessini, M. Longo, C. Masciovecchio, C. Petrillo, A. Radulescu, B. Rossi, et al., Structure of human telomere G-quadruplex in the presence of a model drug along the thermal unfolding pathway, Nucl. Acids Res. 46 (22) (2018) 11927–11938.
[39] S. Di Fonzo, C. Bottari, J.W. Brady, L. Tavagnacco, M. Caterino, L. Petraccone, J. Amato, C. Giancola, A. Cesàro, Crowding and conformation interplay on human DNA G-quadruplex by ultraviolet resonant Raman scattering, Phys. Chem. Chem. Phys. 21 (4) (2019) 2093–2101.
[40] F. D'amico, M. Saito, F. Bencivenga, M. Marsi, A. Gessini, G. Camisasca, E. Principi, R. Cucini, S. Di Fonzo, A. Battistoni, et al., UV resonant Raman scattering facility at Elettra, Nucl. Instrum. Methods Phys. Res. A 703 (2013) 33–37.
[41] D. Fornasiero, T. Kurucsev, Circular dichroism spectra and the interaction between acridine dyes and deoxyribonucleic acid, J. Phys. Chem. 85 (5) (1981) 613–618.
[42] N.V. Anantha, M. Azam, R.D. Sheardy, Porphyrin binding to quadruplexed T4G4, Biochemistry 37 (9) (1998) 2709–2714.
[43] L.R. Keating, V.A. Szalai, Parallel-stranded guanine quadruplex interactions with a copper cationic porphyrin, Biochemistry 43 (50) (2004) 15891–15900.
[44] I. Haq, J.O. Trent, B.Z. Chowdhry, T.C. Jenkins, Intercalative G-tetraplex stabilization of telomeric DNA by a cationic porphyrin, J. Am. Chem. Soc. 121 (9) (1999) 1768–1779.
[45] M. Sirajuddin, S. Ali, A. Badshah, Drug–DNA interactions and their study by UV–Visible, fluorescence spectroscopies and cyclic voltametry, J. Photochem. Photobiol. B: Biol. 124 (2013) 1–19.
[46] E.W. White, F. Tanious, M.A. Ismail, A.P. Reszka, S. Neidle, D.W. Boykin, W.D. Wilson, Structure-specific recognition of quadruplex DNA by organic cations: influence of shape, substituents and charge, Biophys. Chem. 126 (1–3) (2007) 140–153.
[47] V.K. Sharma, P. Sahare, R.C. Rastogi, S. Ghoshal, D. Mohan, Excited state characteristics of acridine dyes: acriflavine and acridine orange, Spectrochim. Acta Part A: Mol. Biomol. Spectrosc. 59 (8) (2003) 1799–1804.
[48] J. Kapuscinski, Z. Darzynkiewicz, M.R. Melamed, Interactions of acridine orange with nucleic acids: properties of complexes of acridine orange with single stranded ribonucleic acid, Biochem. Pharmacol. 32 (24) (1983) 3679–3694.
[49] B.R. Vummidi, J. Alzeer, N.W. Luedtke, Fluorescent probes for G-quadruplex structures, ChemBioChem 14 (5) (2013) 540–558.
[50] T.G. Gantchev, H. Ali, J.E. van Lier, Interactions of chloroaluminium-tetramethyl-tetrapyridino-porphyrazine with DNA, Eur. J. Biochem. 217 (1) (1993) 371–376.
[51] R. del Villar-Guerra, J.O. Trent, J.B. Chaires, G-quadruplex secondary structure obtained from circular dichroism spectroscopy, Angew. Chem. 130 (24) (2018) 7289–7293.
[52] S.P. Fodor, R.P. Rava, T.R. Hays, T.G. Spiro, Ultraviolet resonance Raman spectroscopy of the nucleotides with 266-, 240-, 218-, and 200-nm pulsed laser excitation, J. Am. Chem. Soc. 107 (6) (1985) 1520–1529.
[53] J.R. Perno, C.A. Grygon, T.G. Spiro, Ultraviolet Raman excitation profiles for the nucleotides and for the nucleic acid duplexes poly (rA)-poly-(rU) and poly (dG-dC), J. Phys. Chem. 93 (15) (1989) 5672–5678.
[54] L. Comez, F. Bianchi, V. Libera, M. Longo, C. Petrillo, F. Sacchetti, F. Sebastiani, F. D'Amico, B. Rossi, A. Gessini, et al., Polymorphism of human telomeric quadruplexes with drugs: A multi-technique biophysical study, Phys. Chem. Chem. Phys. 22 (20) (2020) 11583–11592.
[55] J. Palackỳ, M. Vorlíčková, I. Kejnovska, P. Mojzeš, Polymorphism of human telomeric quadruplex structure controlled by DNA concentration: a Raman study, Nucl. Acids Res. 41 (2) (2013) 1005–1016.

[56] J. Palacký, P. Mojzeš, I. Kejnovská, M. Vorlíčková, Does Raman spectroscopy recognize different G-quadruplex arrangements? J. Raman Spectrosc. 51 (2) (2020) 301–312.
[57] E.W. Small, W.L. Peticolas, Conformational dependence of the Raman scattering intensities from polynucleotides. III. Order-disorder changes in helical structures, Biopolym.: Orig. Res. Biomol. 10 (8) (1971) 1377–1418.
[58] B.P. Rosi, V. Libera, L. Bertini, A. Orecchini, S. Corezzi, G. Schirò, P. Pernot, R. Biehl, C. Petrillo, L. Comez, et al., Stacking interactions and flexibility of human telomeric multimers, J. Am. Chem. Soc. 145 (29) (2023) 16166–16175.
[59] F. Würthner, Aggregation-induced emission (AIE): a historical perspective, Angew. Chem. Int. Ed. 59 (34) (2020) 14192–14196.
[60] F. Würthner, T.E. Kaiser, C.R. Saha-Möller, J-aggregates: from serendipitous discovery to supramolecular engineering of functional dye materials, Angew. Chem. Int. Ed. 50 (15) (2011) 3376–3410.
[61] M. Chiriboga, C.M. Green, D. Mathur, D.A. Hastman, J.S. Melinger, R. Veneziano, I.L. Medintz, S.A. Díaz, Structural and optical variation of pseudoisocyanine aggregates nucleated on DNA substrates, Methods Appl. Fluorescence 11 (1) (2023) 014003.
[62] I. Frasson, V. Pirota, S.N. Richter, F. Doria, Multimeric G-quadruplexes: A review on their biological roles and targeting, Int. J. Biol. Macromol. 204 (2022) 89–102.
[63] F. Manoli, F. Doria, G. Colombo, B. Zambelli, M. Freccero, I. Manet, The binding pocket at the interface of multimeric telomere G-quadruplexes: Myth or reality? Chem. Eur. J. 27 (45) (2021) 11707–11720.
[64] R.C. Monsen, J.O. Trent, J.B. Chaires, G-quadruplex DNA: a longer story, Acc. Chem. Res. 55 (22) (2022) 3242–3252.
[65] R. Rigo, E. Groaz, C. Sissi, Polymorphic and higher-order G-quadruplexes as possible transcription regulators: Novel perspectives for future anticancer therapeutic applications, Pharmaceuticals 15 (3) (2022) 373.
[66] V. Pirota, C. Platella, D. Musumeci, A. Benassi, J. Amato, B. Pagano, G. Colombo, M. Freccero, F. Doria, D. Montesarchio, On the binding of naphthalene diimides to a human telomeric G-quadruplex multimer model, Int. J. Biol. Macromol. 166 (2021) 1320–1334.